RSC Advances

PAPER

View Article Online
View Journal | View Issue

Cite this: *RSC Adv.*, 2014, **4**, 31142

Catalytic features of Ni supported on CeO_2–ZrO_2 solid solution in the steam reforming of glycerol for syngas production

Thaisa Aparecida Maia and Elisabete Moreira Assaf*

Catalysts containing 5 wt% Ni supported on $Ce_xZr_{1-x}O_2$ solid solutions prepared by the Pechini method were tested in steam reforming of glycerol (SRG) reactions. The catalysts were characterized by temperature programmed reduction with H_2 (H_2-TPR), XANES with H_2-TPR, X-ray diffraction (XRD) for fresh and used catalysts, XRD *in situ* for reduced catalysts, N_2-physisorption, oxygen storage capacity (OSC), and scanning electron microscopy (SEM). H_2-TPR analysis revealed various degrees of interaction between the NiO phase and the supports, which were confirmed by XANES analysis. XANES data also showed greater reduction of mixed supports, than of pure supports, showing that the presence of Zr^{4+} promotes CeO_2–ZrO_2 reduction. XRD confirmed the formation of CeO_2–ZrO_2 solid solutions, with cubic and tetragonal crystal structures, depending on the composition. N_2 physisorption analysis showed a greater surface area on the CeO_2–ZrO_2 solid solution supports than on the pure supports and this increase may be related to the insertion of ZrO_2 in the CeO_2 lattice. The SRG reaction was performed at 973 K with molar feed ratios of H_2O–glycerol = 3 : 1. All catalysts exhibited catalytic activity for the reaction, but carbon formation was high on the catalysts supported on pure oxide. The 5% Ni50CZ catalyst was the most selective for syngas production in the SRG. In addition to the nickel activity, the experiments revealed the activity of the supports in oxidation reactions, which was assigned to the formation of oxygen vacancies by the interaction of CeO_2 with ZrO_2.

Received 1st April 2014
Accepted 20th June 2014

DOI: 10.1039/c4ra02886d

www.rsc.org/advances

Introduction

The diminution of fossil fuel reserves and the pollution caused by their combustion, combined with the continued rise in energy demands, make hydrogen and syngas (CO + H_2) attractive alternative sources of energy, when they are produced from renewable resources such as alcohols derived from biomass, because they pollute less than most fuels and contribute to reducing global warming and our dependence on fossil fuels.[1]

Syngas production is economically important, this being the highest cost stage in the production of liquid compounds, in the gas-to-liquid (GTL) process. Focusing on this stage, a potential way of producing syngas is the steam reforming of glycerol (SRG). SRG has been studied recently and shown to be a promising process for the production of syngas and/or H_2; furthermore, glycerol is generated in quantities exceeding current needs, as a byproduct of the process of biodiesel production, the transesterification of vegetable oils. According to Reaction (1), up to four moles of hydrogen per mole of glycerol could be formed by simple decomposition. Under steam-reforming conditions, however, the water–gas shift reaction (Reaction (2)) will occur simultaneously:[2]

$$C_3H_8O_3 \leftrightarrows 3CO + 4H_2 \qquad (1)$$

$$3CO + 3H_2O \leftrightarrows 3CO_2 + 3H_2 \qquad (2)$$

Therefore, a maximum of seven moles of hydrogen could be generated in the SRG and the global reaction is presented as:

$$C_3H_8O_3 + 3H_2O \rightarrow 3CO_2 + 7H_2 \qquad (3)$$

Some studies suggest that catalysts used for the steam reforming of ethanol (SRE) reaction may also be active in the SRG, among them stand out from Ni catalysts. Zhang *et al.*[3] studied Co and Ni catalysts for the SRE and SRG processes, noting that these catalysts are significantly active and selective in both reactions. However, they suffered from the disadvantage of carbon formation.[4] Therefore, it is necessary to develop alternative catalysts that form less carbon formation; for example, by using supports that favor the gasification of carbon to CO or CO_2, such as CeO_2 and ZrO_2.

Metallic catalysts supported on CeO_2 and ZrO_2 have been receiving a lot of attention because of several interesting properties of these supports, such as thermal stability, electrical conductivity and oxygen vacancies. In previous work, these supports have been evaluated in steam processes for H_2 or syngas production. CeO_2 has the ability to store and release

---

Instituto de Química de São Carlos – Universidade de São Paulo, Avenida Trabalhador Sãocarlense, 400, São Carlos, SP, Brazil. E-mail: eassaf@iqsc.usp.br

oxygen, participating in the oxidation of CO and hydrocarbons.[5] ZrO_2 may be dissolved in CeO_2 to increase the mobility of oxygen and thermal stability.[6]

Nickel catalysts supported on CeO_2 were tested in SRG by Manfro *et al.*[7] The reaction was carried out in a batch reactor with aqueous solutions of 1 and 10 wt% glycerol, at 523 and 543 K. A maximum glycerol conversion of 30% was achieved at 543 K with 1% glycerol solution. In the gas phase, the mole fraction of H_2 was always higher than 70% and formation of CH_4 was very low (<1%). Increasing the glycerol concentration decreased the rate of conversion and the formation of H_2.

Nichele *et al.*[8] studied the Ni catalysts activity in H_2 production from SRG, analyzing Ni addition and the effect of different supports, such as TiO_2, ZrO_2 and SBA-15. $NiZrO_2$ catalyst showed higher stability and H_2 selectivity at 923 K, concluding thus that this system may be promising for the reaction of SRG and can get good results, according to the reaction conditions used.

Considering the advantages of using nickel as the catalyst for steam reforming reactions and using CeO_2 and ZrO_2 as supports, the objective of study was to investigate nickel catalysts supported on CeO_2–ZrO_2 solid solutions used in SRG reactions for the production of syngas.

Experimental

Preparation of catalysts

The supports were produced by the polymeric precursor method (Pechini method).[9] First, zirconium carbonate (Alfa Aesar) was stirred into a solution of citric acid in ethylene glycol.[9,10] Next, an aqueous solution of cerium ammonium nitrate (Alfa Aesar) was added, to give the following mole fractions of CeO_2 in the final oxides: 0; 0.25; 0.50; 0.75 and 1. The mixture was heated to 383 K and the resin formed was cured at this temperature for 24 h, dried at 393 K for 12 h and calcined in two steps: at 773 K for 2 h (2 K min^{-1}) and 973 K for 3 h (2 K min^{-1}).

Catalysts with 5 wt% Ni were prepared by impregnating the supports with aqueous $Ni(NO_3)_2 \cdot 3H_2O$ (Alfa Aesar) solution at 343 K for 3 h. The solid was then dried in an oven at 333 K for 12 h and finally calcined at 873 K for 3 h.

In this paper, the catalysts $Ni/Ce_xZr_{1-x}O_2$ ($0 < x < 1$) are abbreviated to NiCZ, the supports being referred to as C; Z; 25CZ; 50CZ and 75CZ for ceria, zirconia, 25, 50 and 75% ceria in zirconia, respectively. The catalysts with a nickel load of 5 wt% were thus named 5% NiC, 5% NiZ, 5% Ni25CZ, 5% Ni50CZ and 5% Ni75CZ.

Characterization of catalysts

Characterization for fresh catalysts

H_2 temperature-programmed reduction (H_2-TPR). The TPR analyses were performed in a multipurpose analytical system (SAMP3, Termolab Equipamentos Ltd, Brazil) with a thermal conductivity detector (TCD), a reducing gas mixture of 2% H_2–98% Ar (v/v) and a heating rate of 10 K min^{-1} from 298 to 1273 K.

X-ray absorption near-edge structure spectroscopy (XANES) with H_2 TPR. XANES spectra were collected at the Ni K-edge and Ce LIII-edge, at the D06A – XAS beamline of the Brazilian Synchrotron Light Laboratory (LNLS) in Campinas, Brazil. A Si (1 1 1) polychromator was used to select the X-ray beam from the synchrotron light produced by the 1.37 GeV electron storage ring, at a maximum current of 200 mA. The Ni K-edge and Ce LIII-edge absorption spectra were recorded in the transmission mode with a CCD camera, in a photon energy range from 8200 to 8800 eV for Ni K-edge and from 5500 to 6000 eV for Ce LIII-edge. The oxidized samples were heated, in hydrogen flowing at 30 mL min^{-1}, from 298 to 923 K at 10 K min^{-1} and held at 923 K for 30 min. The XANES spectra at the Ni K-edge and Ce LIII-edge were collected *in situ* during reduction, throughout the temperature range.

X-ray diffraction (XRD). XRD powder patterns were acquired in a Rigaku Multiflex diffractometer, to identify the crystalline phases, with Cu Kα radiation (1.54178 nm). The Bragg angle, 2θ, was scanned between 5° and 80° at 2° min^{-1}.

XRD of activated catalysts: XRD patterns of activated catalysts were recorded *in situ* at the XPD-10B beamline of the LNLS synchrotron radiation facility. The measurements were made in the reflection mode, in a 2θ interval from 25° to 55°, with radiation of $\lambda = 1.54996$ Å, calibrated with a Si (1 1 1) monochromator. The oxidized samples were heated, in a flow of H_2, from 298 K to the temperature of reduction (923 K), at 10 K min^{-1}, and held at that temperature for 1 h and, after that, a diffraction pattern was collected *in situ*.

From the XRD patterns, it was possible to calculate the mean crystal diameter (d) of the particles responsible for the most intense peak, for the supports (d_{support}), NiO phase (d_{NiO}) and metal phase Ni (d_{Ni}), by using Scherrer's formula (eqn (4)):

$$d = \frac{k\lambda}{\beta \cos \theta} \tag{4}$$

where: d = mean crystal size (nm), k = proportionality constant, which depends on the shape of particles, here assumed to be spherical ($k \sim 0.9$), β = width at half height of the most intense peak (radians), λ = wavelength of incident radiation (nm) θ = half the Bragg angle (°).

N_2-physisorption. The specific surface area was estimated with a Quantachrome Nova 1000e analyzer, by applying B.E.T. theory to the N_2 adsorption isotherm.

Oxygen storage capacity (OSC). OSC measurements on the ceria–zirconia oxides were made an apparatus similar to that for TPR, attached to a Quadrupole mass spectrometer (Omnistar QMS200 of Balzers). The sample was reduced in pure H_2 flowing (25 mL min^{-1}) at 923 K for 1 h, than the surface was purged with He (50 mL min^{-1}) at the same temperature for 1 h. After stabilization of the O_2 signal in the mass spectrometer, while passing an O_2 stream (8% O_2: He – 50 mL min^{-1}) in parallel to the reactor (by-pass mode), the O_2 flow was passed through the sample to obtain the breakthrough curve, from which the total OSC was determined. These analyses were performed in the Catalysis and Chemical Processes Laboratory, at the National Institute of Technology (INT), Rio de Janeiro, Brazil.

Characterization for spent catalysts

XRD after SRG reaction. XRD powder pattern for 5% Ni50CZ after reaction were acquired under the same conditions of the fresh catalysts.

SEM analyses. SEM photomicrographs were taken in a ZEISS LEO 440 microscope (Cambridge, England), with an OXFORD detector (7060), operating at 20 kV electron beam. The samples were coated with 10 nm of gold in a BAL-TEC MED020 sputter coating system (BAL-TEC, Liechtenstein) and kept in a desiccator until the time off analysis.

Catalytic tests

The catalytic tests were performed at atmospheric pressure, in a fixed-bed tubular quartz micro-reactor. Prior to the reaction, 150 mg of the catalyst was introduced into the reactor and reduced *in situ* in flowing H_2 (30 mL min^{-1}) at 923 K (10 K min^{-1}) for 1 h, to activate the catalyst. After that, the surface of the catalyst was purged in a flow of pure N_2 at the reaction temperature (973 K). The catalytic bed temperature was controlled with the aid of a thermocouple introduced into the bed. The reaction was started in a hydrogen-free feed, when the N_2 was replaced with water–glycerol in a 3 : 1 molar ratio, flowing at 2.5 mL h^{-1}, supplied by a piston pump. This mixture was vaporized in a preheating chamber (453 K) before reaching the reactor. The gaseous products were analyzed with an in-line gas chromatograph (VARIAN GC-3800) with two columns in parallel, each with a TCD at the outlet. The columns were packed with Porapak-N and 13X Molecular Sieve, operating between 313 K and 353 K, with He and N_2, respectively, as carrier gas, flowing at 10 mL min^{-1}. The liquid products collected at the reaction outlet were analyzed with a gas chromatograph (Shimadzu), with H_2 as carrier gas and HP5 capillary column, operating between 308 K and 523 K. During preparation of the liquid products for GC analysis, the solution was kept at temperature below 283 K, to avoid the evaporation of products.

The glycerol conversions were calculated at the end of the experiments by analyzing the amount of unreacted glycerol contained in the cold trap, and were defined as mole percent of glycerol consumed per mole of supplied reactant.

The catalysts 5% NiC, 5% Ni50CZ and 5% NiZ were also subjected to temperature ramps, to assess the catalytic behaviour of these catalysts at various temperatures and to determine the best temperature at which to work. The product composition was recorded for all catalysts over 6 h on stream at 973 K.

Results and discussion

H_2 temperature-programmed reduction (H_2-TPR)

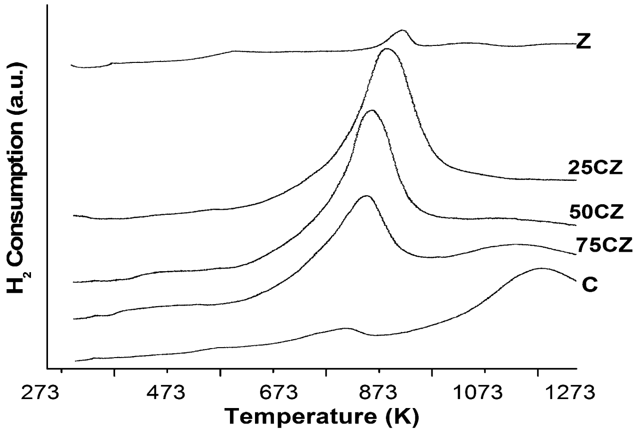

Fig. 1 Reduction profile of supports.

Fig. 1 shows the CeO_2–ZrO_2 reduction profiles of all supports. The TPR profile of C shows two peaks, a small one at 833 K and a stronger peak at 1193 K; this profile is similar to that reported in the literature.[11] The first peak may be associated with oxygen reduction on the surface of CeO_2, which is covered with oxygen anions (O^{2-} or O^-), and the second peak corresponds to the reduction of CeO_2 in the bulk of the material, through the reduction of Ce^{4+} to Ce^{3+} by the removal of O^{2-}anions from the lattice and formation of Ce_2O_3, as follows:[12]

$$2CeO_2 + H_2 \rightarrow Ce_2O_3 + H_2O \tag{5}$$

The reduction of Z occurs at 942 K. This small reduction peak is attributed to $Zr^{4+} \rightarrow Zr^{3+}$, which may occur only on the support surface.[13] In the profiles of mixed supports, 25CZ and 50CZ a single reduction peak is present, characteristic of a single phase. According to the literature,[14] the reduction of a solid solution can be affected by oxygen mobility, which allows the reduction of the bulk of the material at a lower temperature. Indeed, the reduction in the bulk of this solid solution is strongly promoted by the insertion of ZrO_2 into the CeO_2 lattice, as can be observed in Table 1, which shows the H_2 consumption and OSC measurements for the supports. These analyses showed a higher H_2 consumption and higher oxygen storage capacity for 25CZ and 50CZ. The 75CZ support shows an additional a high-temperature peak, unlike 50CZ and 25CZ. This peak may correspond to the reduction of bulk ceria in an inhomogeneous portion of the sample with a higher content of Ce.

Fig. 2 shows the TPR profiles of the catalysts. All the Ni reduction peaks were attributed to the reduction of Ni^{2+} to Ni^0.[15] Previous H_2-TPR investigations indicated that TPR peaks at lower temperatures refer to the reduction of nickel oxide crystallites and, those at higher temperatures can be attributed to nickel species interacting more strongly with the support.[16] All catalysts show broadly similar profiles, with three reduction peaks. However, these peaks are shifted to higher or lower temperatures and vary in relative magnitude, showing more or less interaction between nickel and support.[17] For comparison, the NiO reduction profile is also shown, with a single reduction peak at $T_{max} = 690$ K. Since the supports were reduced over the same temperature range as the nickel species, profiles show co-reduction of NiO and support oxides at these temperatures.

The peak at the lowest temperature (γ) can be attributed to reduction of NiO interacting weakly with the support. This peak corresponds to the reduction of NiO species influenced by

Table 1 Structural characteristics of the CZ supports

				H_2 consumption (mol H_2) × 10^5			
Support	$d_{support}$ (nm)	Lattice parameter[a] (nm)	S_{BET} ($m^2\ g^{-1}$)	Experimental	Theoretical	Reduction (%)	OSC (μmol O_2 per g cat)
C	25.9	0.5394	18.3	1.30 (bulk), 0.80 (surface)	29.0	7.3	265
75CZ	8.4	0.5377	57.6	1.25 (bulk), 4.35 (solid solution)	21.2	25.8	355
50CZ	7.3	0.5322	48.3	8.50	14.5	59.0	419
25CZ	7.8	0.5268	47.9	7.00	7.3	96.8	380
Z	13.2	—	29.3	0.45	40.4	1.1	67

[a] based on the standard lattice parameter of CeO_2: 0.5412 nm.

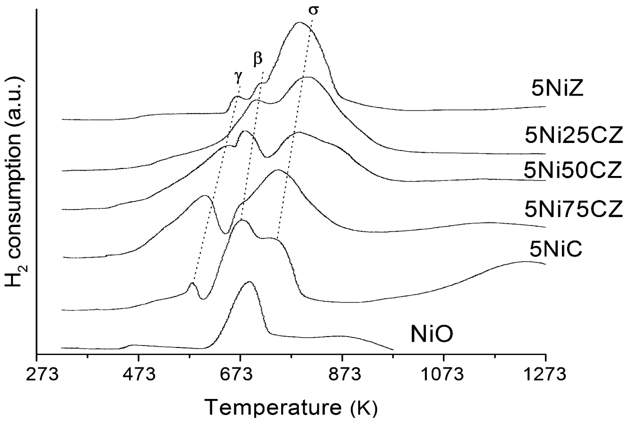

Fig. 2 Reduction profile of catalysts.

oxygen vacancies in the support. This occurs by an initial weakening of the Ni–O bond or polarization of the H_2 molecule, which becomes more reactive for NiO reduction in the neighborhood of oxygen vacancies.[18] The second peak (β) indicates reduction of NiO crystallites (observed by XRD). The third peak (σ) can be attributed to the reduction of NiO species interacting more strongly with the support.

Previous H_2-TPR investigations pointed out that the main features of CeO_2–ZrO_2 supports are the creation of oxygen vacancies as the solid solution is formed and the effect on the redox behavior of the interaction between these vacancies and the supported catalytic oxides.[19] Not only does the solid solution influence the NiO reduction, but also the NiO particles apparently facilitate the reduction of CeO_2–ZrO_2 through the H_2 spillover effect during TPR or activation.[20] This process can be explained in various ways: the H_2 molecule may be dissociated and adsorbed on NiO and hydrogen atoms can then be distributed on to the CeO_2–ZrO_2. Another possibility is that the H_2 is activated at the contact point between NiO and solid solution particles. A third explanation is that the hydrogen spillover effect could occur from a small number of Ni sites formed on the NiO surface, but not be detected by TPR.[20] The amounts of H_2 consumed in each TPR experiment are shown in Table 1. It is seen that the support that led to the highest H_2 consumption was 50CZ. From this result, it is assumed that this higher consumption may be associated with a greater number of vacancies in the support, which could also be related to the higher OSC for this support.

XANES with H_2-TPR

XANES *in situ* analyses during H_2 TPR are very useful, as they show the variation in electronic properties of the Ni atoms during the reduction process. For this purpose, the most relevant features of XANES spectra are the intensity of the white line and pre-edge structures.[21,22] XANES spectra of two of the catalysts studied are shown in Fig. 3. Reference spectra of NiO and metal Ni are presented in Fig. 4, representing the oxidation states Ni^{2+} and Ni^0 respectively. It can be verified that all the samples gave profiles similar to that of NiO at lower temperatures, with the same white line at 8350 eV, and that this white line is caused by Ni–O interaction.[23–25] When the catalysts are heated in a flow of H_2, it is found that the intensity of the white line falls, so that the spectrum takes on a profile similar to that of metallic Ni, while the intensity of the pre-edge signal at 8330 eV rises. These are results show the reduction of Ni(II) to Ni^0,[26] confirming the TPR analyses. It is observed that, corroborating results obtained by TPR, the reduction of Ni species starts around 623 K and, by 823 K, is complete in all catalysts.

Fig. 5 and 6 show XANES spectra recorded at the Ce L^{III} edge for 5% NiCZ catalysts, during H_2 TPR. The analyzes were performed from room temperature to 923 K. At room temperature, the spectrum corresponds to Ce^{4+} species and a double white line was observed (named B and C). Due to the crystal field splitting for the 5d level of Ce, these peaks were assigned to $2p_{3/2}/(4f^1L)5d^1$ and $2p_{3/2}/(4f^0)5d^1$ transitions, respectively. The "L" denotes that an electron in the 2p orbital of oxygen is transferred to the 4f orbital of a Ce atom and $5d^1$ refers to the excited electron in the unoccupied 5d state.[27,28]

The increasing temperature of the TPR program causes changes in peaks B and C in the 5% NiCZ spectra. There is a decrease in the intensity of C band and displacement of band B to lower energies (indicated as A in Fig. 6).

For the 5% NiC catalyst, the two peaks B and C, corresponding to Ce^{4+}, do not change, but, with the addition of Zr to the supports, the higher energy peak loses intensity and reduction profiles of catalysts supported on mixed oxides show a band A corresponding to the oxidation state Ce^{3+}, indicating a mixture of two oxidation states, Ce^{3+} and Ce^{4+}. For the catalysts with higher Zr content, peak A, due to the dipole-allowed

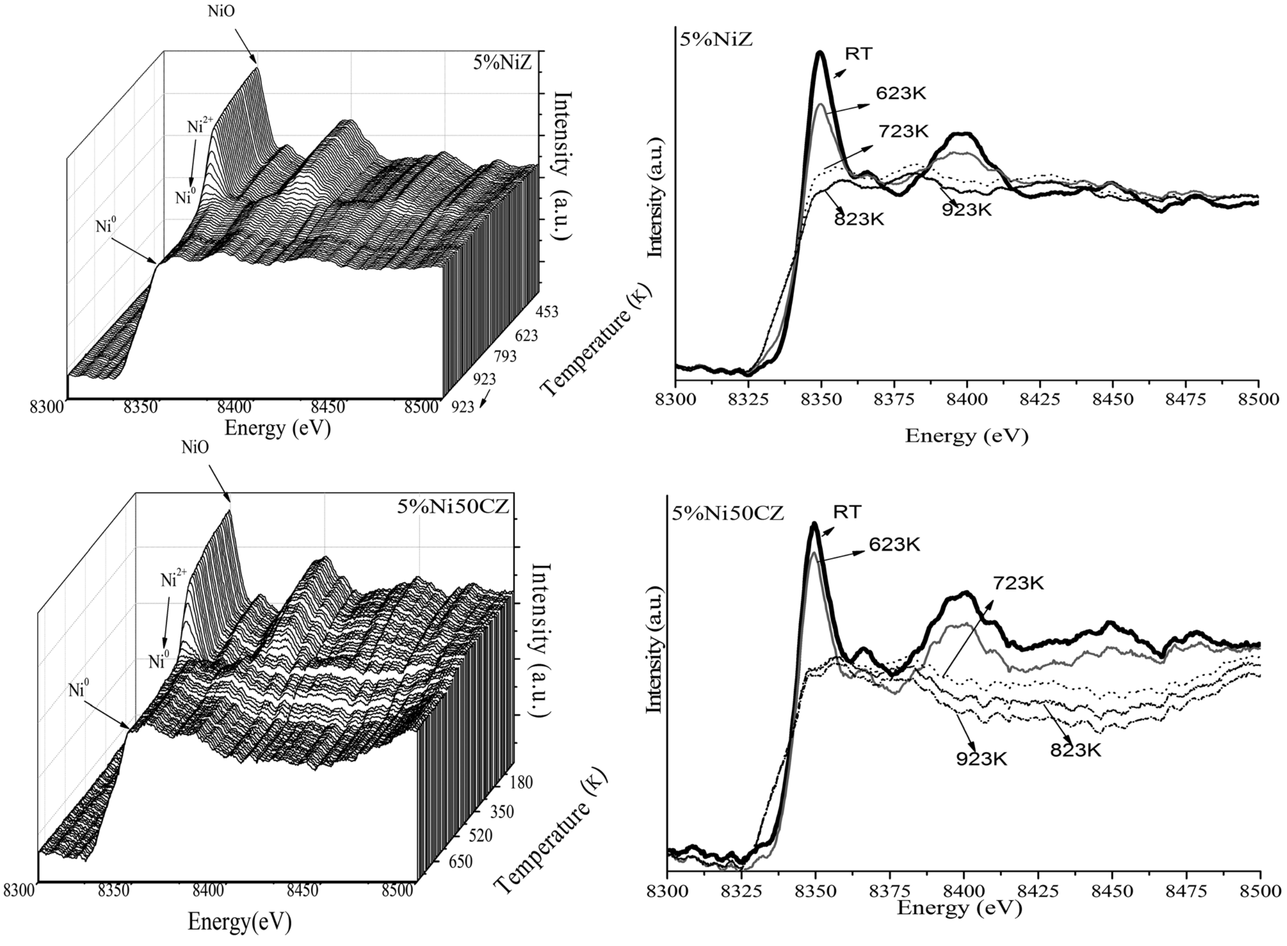

Fig. 3 *In situ* XANES-H_2 TPR spectra of the catalysts (a) 5% NiZ and (b) 5% Ni50CZ, at the NiK absorption edge.

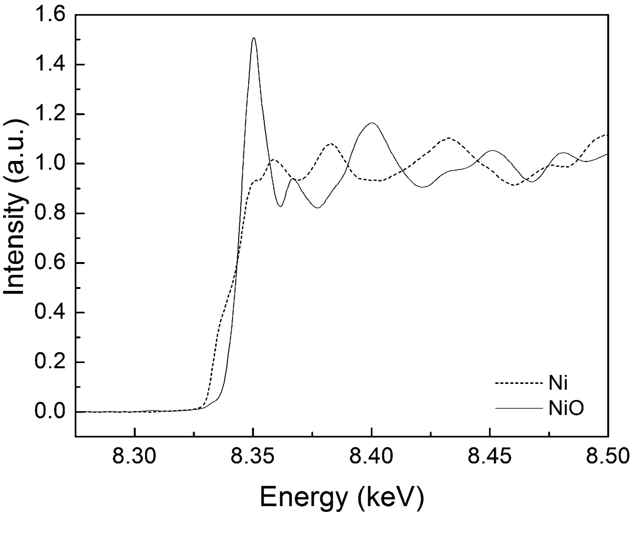

Fig. 4 XANES spectra of reference compounds (metallic Ni and NiO).[22]

transition $2p_{3/2} \rightarrow (4f^1)5d$,[29,30] which characterizes the Ce^{3+} oxidation state, is more intense and thus the addition of Zr is correlated with a higher reducibility in mixed support.[27,31] As observed in the TPR-H_2 profiles of the supports, the addition of Zr promotes CeO_2–ZrO_2 reduction at lower temperatures, besides increasing the extent of reduction, which increases with increasing Zr content, as confirmed by XANES-H_2 TPR analysis (Fig. 7).

X-ray diffraction (XRD)

Fig. 8 and 9 present the X-ray diffraction patterns of the supports and catalysts. These were compared with published patterns.[32] The pattern of support C showed diffraction peaks at Bragg angles $2\theta = 28.6$, 36.1, 47.4, 56.4, 59.2, 69.4, 76.7 and 79.4°, characterizing support C as a crystalline Ce oxide with a cubic fluorite structure (JCPDS 81-0792). The XRD pattern of the support Z showed peaks at $2\theta = 17.43$, 24.17, 28.28, 31.65, 34.49, 35.33, 38.65, 40.90°; 45.60, 50.44, 54.16, 55.36, 62.82 and 65.79° (JCPDS 83-0944), characteristic of the ZrO_2 monoclinic structure, besides three main diffraction peaks of the tetragonal structure of this oxide at $2\theta = 30.38$, 59.26 and 60.37° (JCPDS 79-1768).[33]

In the XRD patterns of the mixed oxides, the main peak at $2\theta = 28.6$, ascribed to the ceria structure, shifts to higher angles as ZrO_2 is added, indicating the formation of solid solution. This is due to the insertion of Zr^{4+} ions in the crystal lattice of CeO_2, which causes a change in the lattice parameter (Table 1). The

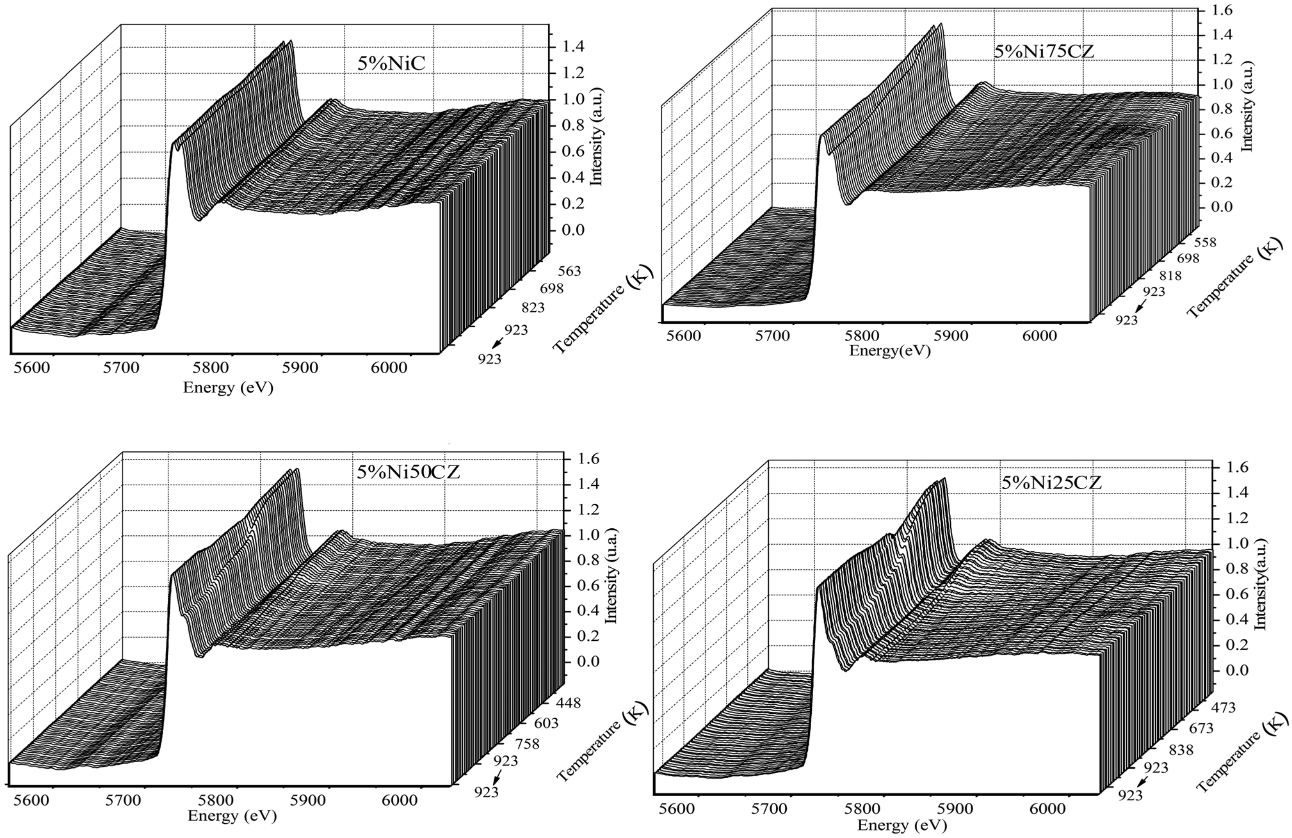

Fig. 5 *In situ* XANES-H_2 TPR spectra of the 5% NiCZ catalysts at the Ce L^{III} absorption edge.

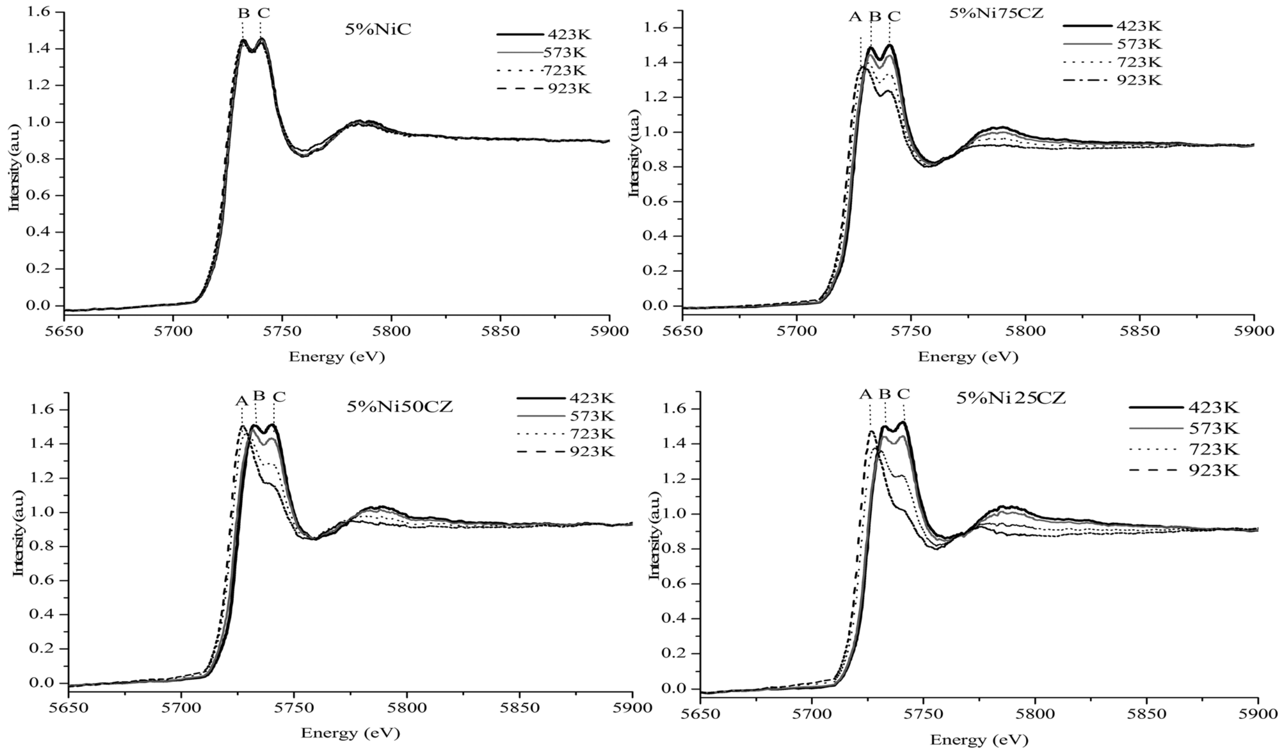

Fig. 6 Selected XANES *in situ* spectra at the Ce L^{III} absorption edge for 5% NiCZ catalysts undergoing H_2 TPR.

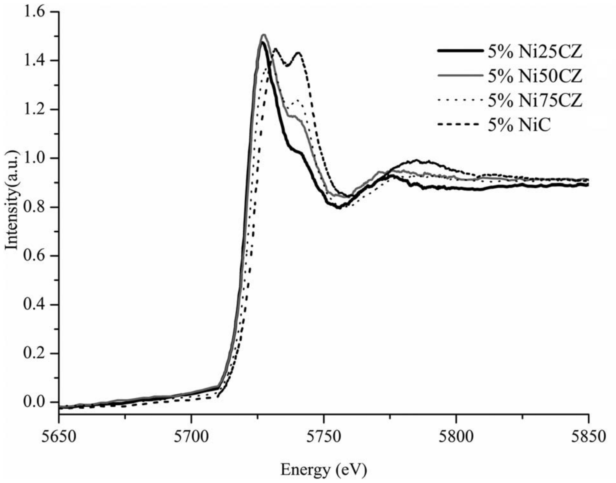

Fig. 7 Comparison of the XANES-H_2 TPR *in situ* spectra reduction of catalysts at 923 K – influence of Zr addition in the support reduction.

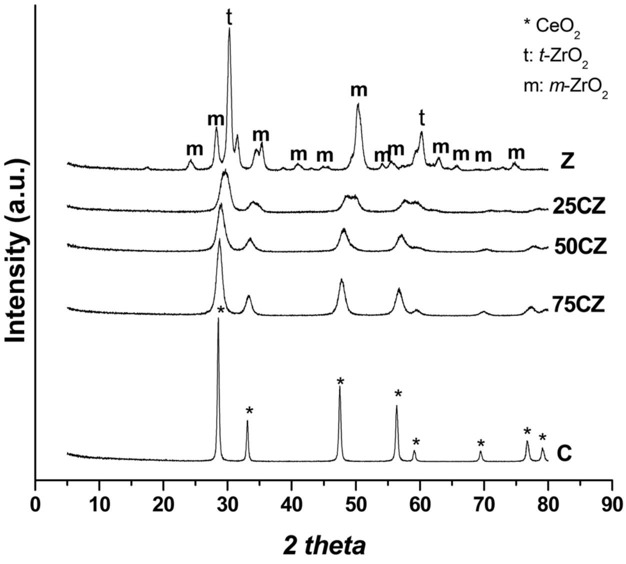

Fig. 8 X-ray diffractograms of supports.

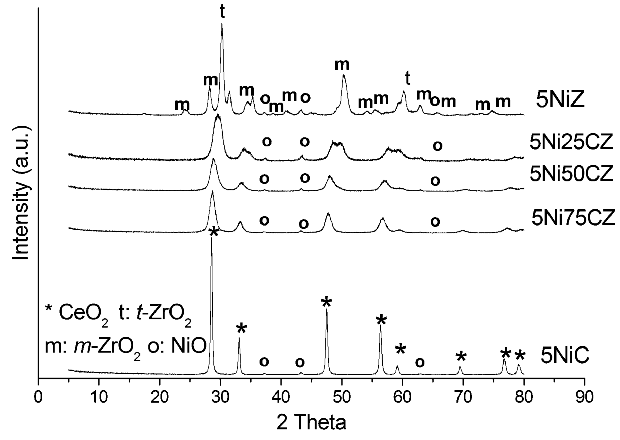

Fig. 9 X-ray diffractograms of catalysts.

insertion of increasing amounts of Zr^{4+} into the cubic fluorite structure decreases the cell volume because of the smaller ionic radius of Zr^{4+} (0.84 Å), with relative to that of Ce^{4+} (0.97 Å), leading to progressive shrinkage of the lattice parameter.[34] The crystal structure of the solid solution depends on the composition. For the supports with higher Ce content, the diffractograms show a profile closer to the cubic fluorite structure of CeO_2, with a shift in 2θ consistent with the insertion of Zr^{4+} mentioned above. Higher contents of zirconia transform the structure to tetragonal.[33]

Besides the diffraction peaks of the supports, the XRD patterns of the catalysts (Fig. 9) also show weak diffraction peaks at Bragg angles $2\theta = 37.29$; 43.29 and 62.96°, which are characteristic of the NiO phase (JCPDS 44-1159).

Structural characteristics of the supports and catalysts

Table 1 summarizes some structural characteristics of the supports, such as mean crystallite diameter, BET surface areas, H_2 consumption in TPR and OSC, determined by the techniques of X-ray diffraction, N_2 physisorption, temperature programmed reduction and oxygen storage capacity. It was observed that Zr^{4+} addition led to a reduction in the crystallite size (d_{support}). These smaller values can be interpreted as a result of loss of crystallinity with solid solution formation.[35] It is observed that the reduced crystallite size in mixed oxide supports has resulted in an increase in BET surface area, suggesting that the addition of zirconium to the solid solution leads to textural changes.

H_2 consumption values were calculated from TPR profiles, considering the experimental and theoretical H_2 consumption. It is observed that these values are correlated with the surface area of the supports. For the C support, it is apparent that the H_2 consumption corresponding to surface reduction is less than the H_2 consumption calculated for the bulk reduction, is typical behavior of low-surface-area materials, also indicating that the reduction of support C begins on the surface and progressively affects the bulk region.[12] The Z support showed a low level of reduction, also reported by other authors.[13,36,37]

The H_2 consumption by the mixed oxides was higher than that by the pure oxide supports. This higher consumption could be related to the greater BET surface area and to the solid solution composition. A higher BET surface area favors the availability of cerium at the surface and consequently a higher H_2 consumption. Moreover, the insertion of zirconium can facilitate oxygen transport from bulk to the surface, facilitating the solid solution reduction.[6,12]

The H_2 consumption and oxygen storage capacity (OSC) data also agree. A higher consumption of H_2 was accompanied by a greater OSC. According with Gutierrez-Ortis *et al.*,[37] reduction in the mixed oxide of cerium is as follows:

$$\mathrm{Ce}_x\mathrm{Zr}_{1-x}\mathrm{O}_2 + \delta_{\mathrm{H}_2} \leftrightarrows \mathrm{Ce}_x\mathrm{Zr}_{1-x}\mathrm{O}_{2-\delta} + \delta_{\mathrm{H_2O}} + \mathrm{V_o}$$

Through the reduction of cerium, oxygen ions are removed from the surface (oxygen being eliminated by the formation of H_2O molecules), leading to the formation of oxygen vacancies

(V_o). The presence of these vacancies greatly boosts the oxygen mobility from the bulk to the surface. Thus, it is possible to relate the reduction process, vacancy formation, the mobility of oxygen and thus the OSC of the supports. Observing the H_2 consumption and OSC data, it is apparent that the 50CZ and.

25CZ supports have greater mobility of oxygen than the others.

Table 2 summarizes some structural properties of 5% Ni/CeO_2–ZrO_2 catalysts, such as NiO crystallite size, BET surface area and H_2 consumption. The crystallite sizes (d_{NiO}) were calculated by the Scherrer equation from the main peak of the nickel phase present in the diffraction pattern ($2\theta = 43.3°$).

Comparing the surface areas analysis in Tables 1 and 2, it appears that the catalysts have less adsorption capacity than the supports. This is due to the nickel oxide coating on the support surface and obstruction of the pores.

Through the values of NiO crystal size (d_{NiO}) for all catalysts, it can be seen that they decrease with increasing amounts of Zr^{4+} in the support, indicating that the NiO is finely dispersed on the support, perhaps due to greater NiO interaction with the solid solution, promoted by zirconia. The XRD *in situ* analyses were performed for 5% NiC and 5% Ni50CZ catalysts. After reduction, the nickel species present on both supports was in the form of metallic Ni, and its calculated crystal size (d_{Ni}), based on the peak at $2\theta \sim 44.0°$, was 27.0 nm for 5% NiC and 20.7 nm for 5% Ni50CZ, from which it can be confirmed that the ceria–zirconia solid solution enhanced dispersion of the nickel species on the support.[38]

The H_2 consumption showed that all catalysts had a nickel phase reduction over 80%. The literature reports that NiO reduction is influenced by the Ni–Ce interaction. Hydrogen might be dissociatively adsorbed on NiO and hydrogen atoms spilled over to CeO_2–ZrO_2 particles, or hydrogen could be activated at the contact point of between the NiO and solid solution particles. However, from the H_2 consumption data, a correlation cannot be established between the composition of the solid solution and nickel reducibility.[17]

Catalytic tests

Catalytic activity was assessed for 5% NiZ, 5% NiC and 5% Ni50CZ catalysts, at temperatures varying between 673 K and 973 K (Fig. 10). The gas products obtained were typically a reformed gas mixture obtained by reforming oxygenated hydrocarbons. It has been reported that, similarly to the reforming of other alcohols and hydrocarbons, the following reactions may occur in the steam reforming of glycerol.[2,8,38]

$$C_3H_8O_3 \leftrightarrows 3CO + 4H_2 \tag{1}$$

$$C_3H_8O_3 + H_2O \rightarrow CO_2 + 2CO + 5H_2 \tag{6}$$

$$CH_4 + H_2O \leftrightarrows CO + 3H_2 \tag{7}$$

$$CH_4 + CO_2 \leftrightarrows 2CO + 2H_2 \tag{8}$$

$$2CO \rightarrow CO_2 + C \tag{9}$$

$$C_2H_4 \rightarrow \text{polymers} \rightarrow C \tag{10}$$

Reactions at 673 K showed low conversion rates to gaseous products, when compared to higher temperatures. Condensed reaction products were yellowish in color and gas chromatography analysis identified unsaturated compounds (not quantified). The GC-MS analyses at this temperature identified large amounts of the following liquid products: acetic acid, 1,2,3-butanetriol, 1,2-propanediol, propanal and butanoic acid. These results of GC-MS analyses corroborate with Buffoni *et al.*[4]

Metallic Ni favors C–C bond cleavage in the glycerol molecule, leading to CO and H_2 formation. However, on thermodynamic grounds, the steam reforming reaction, being endothermic, is limited at lower temperatures, favoring the formation of liquid products. Besides this, it was observed that a high pressure-drop developed in the reactor, due to the deposition of carbon in the catalytic bed and consequent catalyst deactivation. The precursor of this carbon may be ethylene, formed by dehydration of glycerol.[3,4] The ethylene may be formed after an initial C–C bond cleavage, forming the radicals $CH_2(OH)$–$CH(OH)$ and CH_2–OH, which subsequently evolve towards the formation of C_2H_4, H_2 and CH_4.[8,39,40]

As expected, increasing temperature led to a rise in gas product yields, mainly favouring the formation of H_2 and CO, which was highest at 973 K. A high reaction temperature enhanced both the reforming reaction and the decomposition of glycerol, producing more H_2, CO and CO_2, as seen in Fig. 10.[38] Methane is stable in the system at the lower temperatures, but its content decreases strongly as the temperature rises, owing to the steam and dry reforming of CH_4 (Reactions (7) and (8)). Another product that is not favoured in the highest temperature is CO_2. Above 873 K, it is probable that the increasing influence

Table 2 Structural properties of 5%NiCZ catalysts

			H_2 consumption (mol H_2) × 10^5		
Catalyst	d_{NiO}(nm)	S_{BET} (m^2 g^{-1})	Experimental	Theoretical	Reduction (%)
5% NiC	28.8	16	7.5	8.7	86.2
5% Ni75CZ	26.8	51	7.8	8.5	91.8
5% Ni50CZ	21.8	36	7.0	8.5	82.3
5% Ni25CZ	18.2	42	6.9	8.8	78.4
5% NiZ	13.3	25	8.3	8.7	95.4

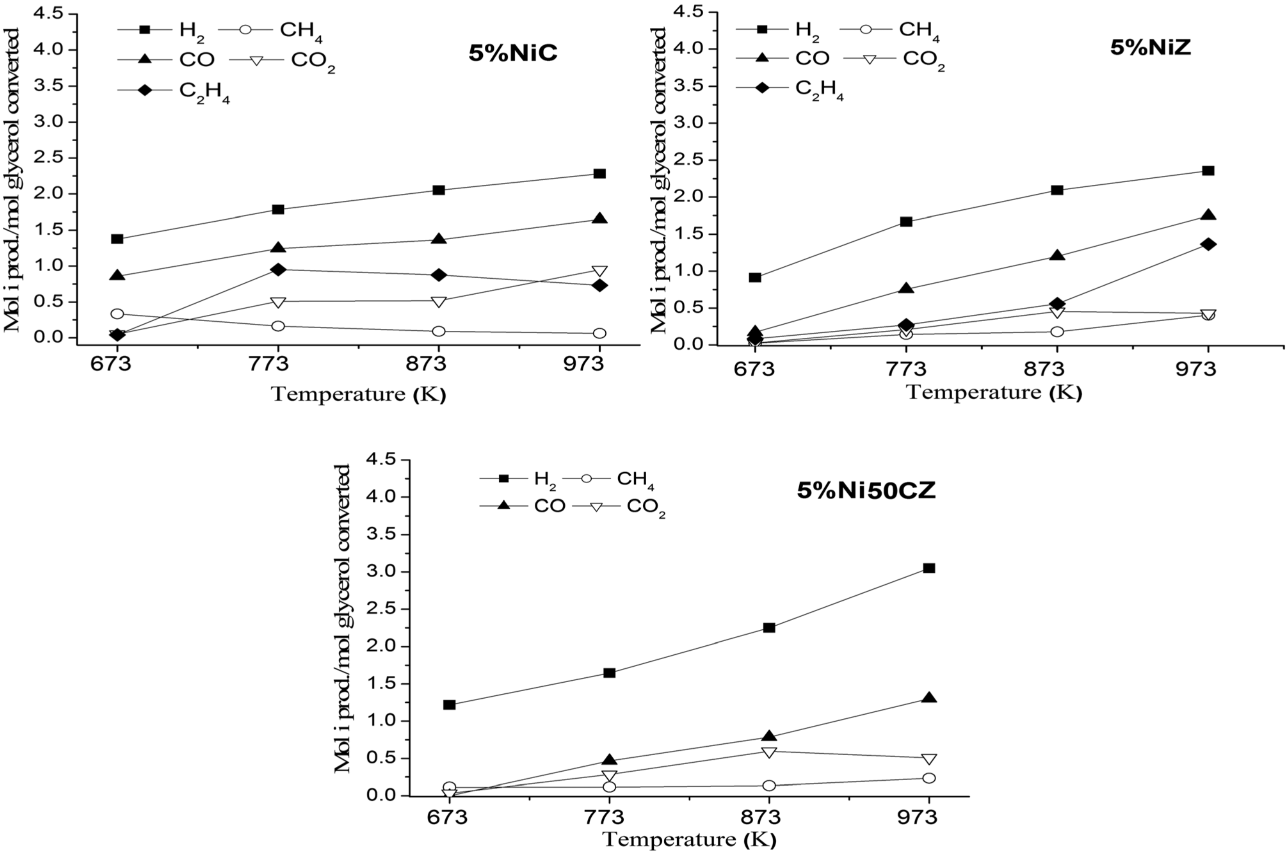

Fig. 10 Influence of temperature on the gaseous products of SGR catalyzed by 5NiC; 5Ni50CZ and 5NiZ.

of the reverse water–gas shift reaction (Reaction (2)) and/or the dry reforming of methane reduces the amount of CO_2.[2] The increase in CO and H_2 yields with rising temperature may also be due to glycerol decomposition (Reaction (1)).

In view of the better performance of the catalysts at higher temperatures, all catalysts were tested over 6 hours at 973 K. Fig. 11 and Table 3 present the results of the catalytic tests. Under these conditions, complete glycerol conversion occurred on all catalysts. In the most of catalysts, the H_2 formation decreased during the reaction, accompanied by an increase in ethylene formation and possible catalytic deactivation (Reaction (10)).[3,4]

Fig. 11 shows the time profiles of the GSR reactions for all the 5% NiCZ catalysts and Table 3 shows the mean selectivity of gaseous products formed on these catalysts during the time on stream. For all catalysts, the CO formation was greater than CO_2 formation.[41] Thus, it is likely that the influence of the reverse water–gas shift reaction is strongest at this temperature, which is consistent with the thermodynamics of the process. This higher CO formation was accompanied by low CH_4 formation, indicating the parallel occurrence of the steam and dry methane reforming reactions (Reaction (7) and (8)) and the activity of these catalysts for these reactions at 973 K, in accordance with studies of Ni catalysts supported on various supports, which showed methane reforming activity.[42,43] Another reason for the lower CH_4 formation is to the fact that the methanation reaction (reverse of Reaction (7)) is exothermic reaction, and thus, at higher temperature, methanation is unfavoured, resulting to a decrease in CH_4 yield at equilibrium.[41]

Among the catalysts analyzed, it was found that 5% Ni50CZ was the most stable during the time of reaction, besides achieving the best H_2, CO and CO_2 formation (favoring Reactions (1) and (6)) and a low carbon deposit (Table 3). This higher activity and stability may be related to its structural properties. This catalyst showed a mixture of crystalline phases (cubic and tetragonal) in the support, according to the XRD analysis. The incorporation of Zr^{4+} in the CeO_2 lattice may lead to a structural distortion, which promotes easier reduction of the support and thus a higher activity for the 50CZ solution than for pure C and Z supports. In the characterization analyses of this catalyst, it was observed that the addition of Zr^{4+} favored a high support reduction in H_2 TPR and oxygen storage capacity. The high activity and selectivity for H_2, CO and CO_2 on 5% Ni50CZ might be due to the OSC. OSC is a important factor to SRG reaction because a higher OSC indicates a better oxygen mobility, which helps in gasifying the coke deposited on the catalyst during the reaction and thus keeps the catalyst active.[41,44]

Besides the structural change, another factor that may promote the higher activity of this catalyst is a strong interaction between Ni and support. The addition of Zr^{4+} addition also promotes a better nickel dispersion on the support and consequently a reduced nickel mean crystal size for 5% Ni50CZ,

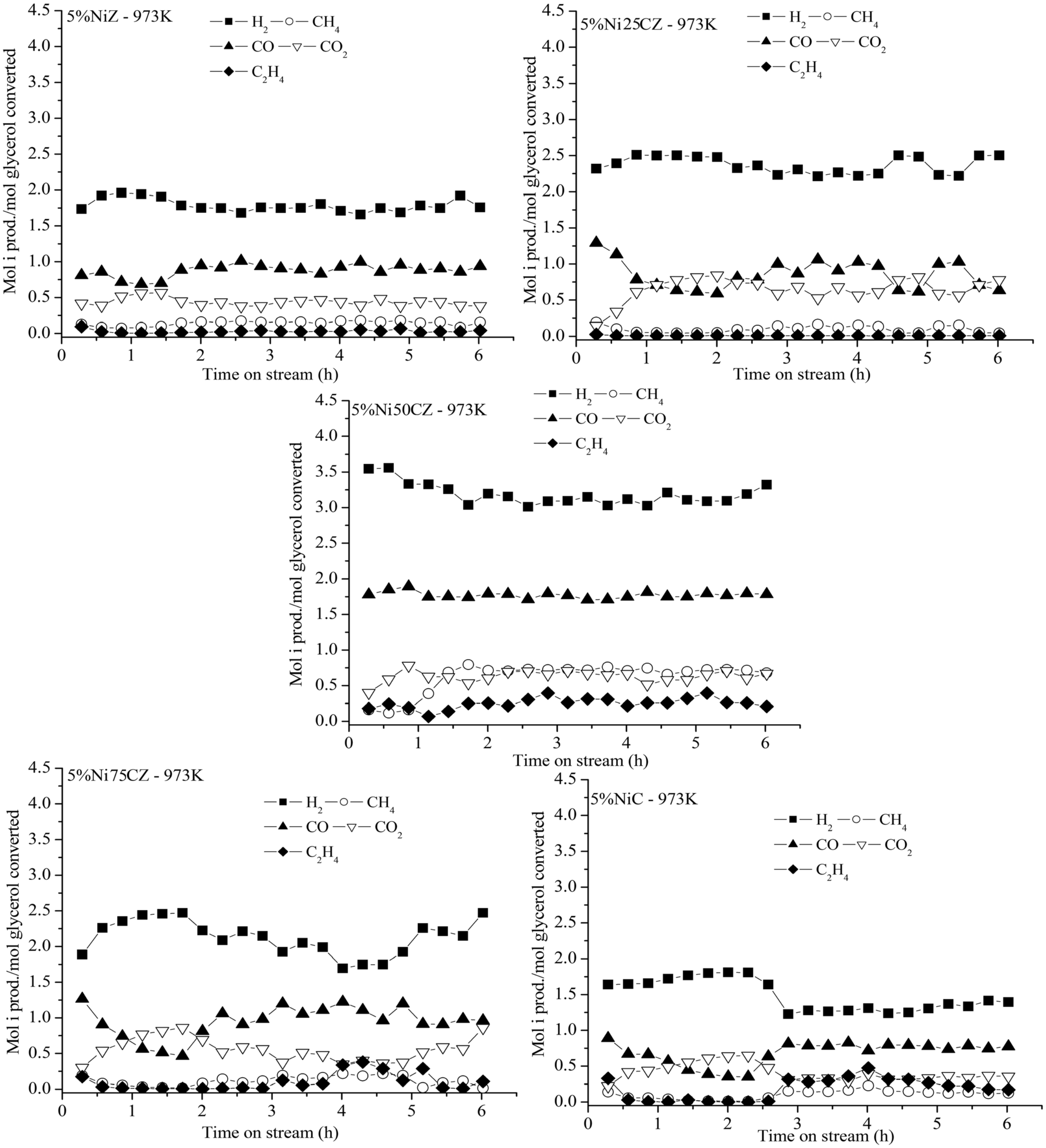

Fig. 11 Gaseous product yields over 6 h of the steam reforming of glycerol at 973 K.

compared to 5% NiC, as was observed in the *in situ* XRD analyses. This better dispersion implies stronger interaction and more intimate contact between Ni and support, improving the probable oxygen transfer from support to Ni.[41,45] According to Takeguchi *et al.*,[20] the interaction between nickel species and oxygen vacancies may create active Ni–Ce^{3+} centers (synergistic effect). This interaction may increase catalytic activity, since the vacancies activate the oxygen species.

The analysis of carbon formation presented in (Table 3) shows a considerably heavier deposit in the 5NiZ catalyst and the gaseous product results show that this catalyst formed less H$_2$, CO and CO$_2$ and more ethylene and CH$_4$, than the other catalysts. Thus, this catalyst undergoes greater deactivation by carbon formation, probably through Reactions (9) and (10). Carbon formation was also great on 5% NiC, and this catalyst also formed a large amount of ethylene. On the mixed supports,

Table 3 Gaseous products and carbon formation of the steam reforming glycerol on 5% NiCZ catalysts at 973 K for 6 h

Catalyst	Gaseous products (mol prod./mol glycerol converted)					Carbon (mmol h^{-1})
	H_2	CH_4	CO	CO_2	C_2H_4	
5NiZ	0.96	0.25	0.96	0.11	1.22	3.11
5Ni25CZ	1.29	0.05	0.65	0.37	0.37	0.42
5Ni50CZ	3.05	0.21	1.33	0.77	—	0.78
5Ni75CZ	1.97	0.17	1.03	0.58	1.19	1.51
5NiC	2.51	0.14	1.00	0.63	1.37	1.64

carbon formation decreased with increasing Zr^{4+} in the solid solution.

According to the literature,[46–48] $Ce_xZr_{1-x}O_2$-supported catalysts show more resistance to carbon formation than those on pure CeO_2 and ZrO_2, because incorporation of Zr^{4+} in the CeO_2 lattice can promote oxygen species reduction, both at the surface and in the bulk of the solid solution, which would favor oxidation reactions, and result in carbon gasification.

Characterization of spent catalyst after the SRG reaction

On the basis of the results of the catalytic tests, further characterization of the catalyst with the best performance (5% Ni50CZ) was carried out after the reaction. The carbon formed on the used catalysts was subjected to XRD and SEM analysis. Fig. 12 shows the XRD patterns for fresh and used catalyst. In the second pattern, the metallic Ni^0 phase is seen at $2\theta \sim 44°$ and $52°$, indicating that the nickel remained totally or partially reduced in the catalytic test. Besides the diffraction peaks for phase, the XRD pattern of the 5% Ni50CZ used catalyst also shows more defined peak and intense diffraction peaks at Bragg angles $2\theta \sim 25.8$, 36.6, 40.3, 42.5 and 68.1°, which are characteristic of carbon graphite (JCPDS 898487).

In addition to the XRD, SEM photomicrograph of fresh and used catalyst are presented in Fig. 13. Fig. 13A shows the photomicrograph of the fresh catalyst and, it can be seen that the surface of the catalyst consists of large particles with a semi-spherical tendency. This catalyst, after the SRG reaction (Fig. 13B), shows the carbon filaments formed on the catalyst surface. The diffractogram for this catalyst after reaction (Fig. 12) also indicated carbon graphite formation, with high crystallinity. Carbon graphite is not easily detected by SEM, but filamentous carbon nanotube structures can be seen in the SEM images.

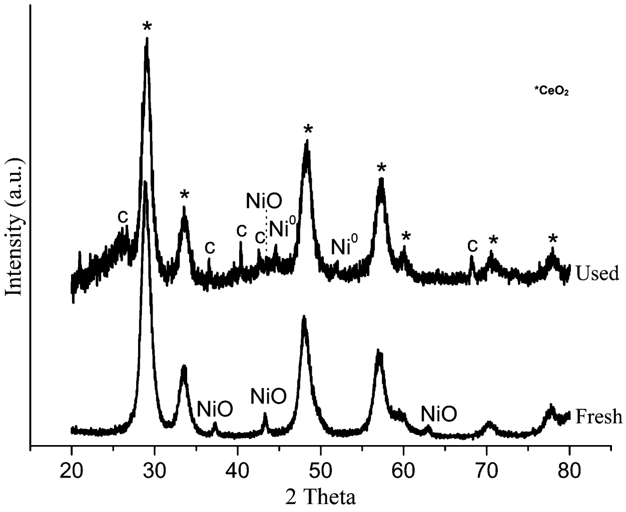

Fig. 12 XRD of used and fresh 5% Ni50CZ.

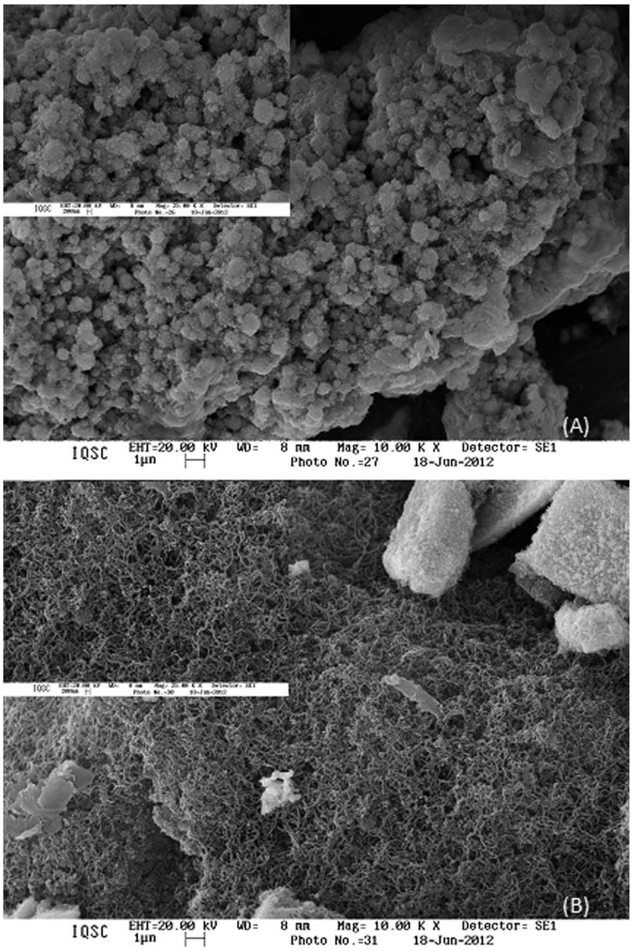

Fig. 13 SEM image of (A) fresh and (B) used 5% Ni50CZcatalyst.

As already reported,[49,50] the presence of species such as NiO crystallites that interact weakly with the support (free NiO), is responsible for the carbon formation on nickel catalysts. Thus, this kind of free NiO, identified in the TPR profile of the catalyst 5% Ni50CZ in Fig. 2 (peak γ) may favour the formation of carbon filaments on this catalyst. However, the formation of carbon filament does not affect the catalytic activity, but results in the variation of the catalytic bed by obstruction.

The catalytic test for SRG on 5% Ni50CZ showed high CO formation, which may be related to the carbon formation. Small NiO crystallites may promote the formation of filamentous carbon at a low growth rate, as may the more dispersed Ni particles, due to a low driving force for diffusion of carbon through the crystallites.[49] This continuous formation of carbon may then be accompanied in part by carbon gasification, leading to the higher formation of carbon monoxide.

Conclusions

The present results show that increasing the reaction temperature in the steam reforming of glycerol favors the formation of CO and H_2, while lower temperatures lead to catalyst deactivation, possibly by the formation of carbon. The incorporation of Zr^{4+} into the CeO_2 lattice leads to a structural change in the mixed oxides and favors reduction of oxide with increasing of Zr content. This structural change, together with a stronger nickel–support interaction, causes the 5Ni50CZ catalyst to be the most stable during the SRG reaction, favoring increased formation of H_2 and CO and reduced carbon formation at 973 K. For this catalyst, it was also observed that the CeO_2–ZrO_2 combination favors the removal of carbon deposits, owing to the increased mobility of oxygen in the solid solution. Considering these results, it was concluded that the association between nickel and CeO_2–ZrO_2 solid solution presents a promising catalytic system for SRG.

Acknowledgements

The authors acknowledge Brazilian federal and state funding agencies CNPQ and FAPESP for financial assistance, the LNLS (Brazilian Synchrotron Light Source Laboratory) for the XANES facilities (DXAS beamlines) and the researcher Marco André Fraga of National Institute of Technology (INT-Rio de Janeiro, Brazil) for Oxygen Capacity Storage (OSC) analyses.

Notes and references

1 L. C. Lima and T. N. Veziroglu, *Int. J. Hydrogen Energy*, 2001, **26**, 39–45.
2 Y. Cui, V. Galvita, L. Rihko-Struckmann, H. Lorenz and K. Sundmacher, *Appl. Catal., B*, 2009, **90**, 29–37.
3 B. Zhang, X. Tang, Y. Li, Y. Xu and W. Shen, *Int. J. Hydrogen Energy*, 2007, **32**, 2367–2373.
4 I. N. Buffoni, F. Pompeo, G. F. Santori and N. N. Nichio, *Catal. Commun.*, 2009, **10**, 1656–1660.
5 R. G. Rao and B. G. Mishra, *Bull. Catal. Soc. India*, 2003, **2**, 122–134.
6 S. Letichevsky, C. A. Tellez, R. R. Avillez, M. I. P. Silva, M. A. Fraga and L. G. Appel, *Appl. Catal., B*, 2005, **58**, 203–210.
7 R. L. Manfro, A. F. Costa, N. F. P. Ribeiro and M. M. V. M. Souza, *Fuel Process. Technol.*, 2011, **92**, 330–333.
8 V. Nichele, M. Signoretto, F. Menegazzo, A. Gallo, V. Dal Santo, J. Cruciani and G. Cerrato, *Appl. Catal., B*, 2012, **111–112**, 225–232.
9 M. P. Pechini, Sprague Electric Co., *US Pat.* 3330697, 26 Aug 1963.
10 P. J. B. Marcos and D. Gouvêa, *Ceramica*, 2004, **50**, 38–42.
11 A. Holmgren and B. Andersson, *J. Catal.*, 1998, **178**, 14–25.
12 S. Damyanova, K. Pawelec, K. Arishtirova, M. V. Martinez-Huerta and J. L. G. Fierro, *Appl. Catal., A*, 2008, **337**, 86–96.
13 W. P. Dow, Y. P. Wang and T. J. Huang, *J. Catal.*, 1996, **160**, 155–170.
14 E. Beryariva, P. Fornasiero, J. Kaspar and M. Graziani, *Catal. Today*, 1998, **45**, 179–183.
15 J. D. A. Bellido and E. M. Assaf, *J. Power Sources*, 2008, **177**, 24–32.
16 M. Diskin, R. H. Cunningham and R. M. Ormerod, *Catal. Today*, 1998, **46**, 147–154.
17 S. Xu and X. Wang, *Fuel*, 2005, **84**, 563–567.
18 J. B. Wang, Y. L. Tai, W. P. Dow and T. J. Huang, *Appl. Catal., A*, 2001, **218**, 69–79.
19 M. H. Youn, J. G. Seo, K. M. Cho, S. Park, D. R. Park, J. C. Jung and I. K. Song, *Int. J. Hydrogen Energy*, 2008, **33**, 5052–5059.
20 T. Takeguchi, S. Furukawa and M. Inoue, *J. Catal.*, 2001, **202**, 14–24.
21 L. P. R. Profeti, E. A. Ticianelli and E. M. AssaF, *Int. J. Hydrogen Energy*, 2009, **34**, 5049–5060.
22 L. P. R. Profeti, J. A. C. Dias, J. M. Assaf and E. M. Assaf, *J. Power Sources*, 2009, **190**, 525–533.
23 J. Juan-Juan, M. C. Román-Martínez and M. J. Illán-Gómez, *Appl. Catal., A*, 2004, **264**, 169–174.
24 S. Takenaka, E. Kato, Y. Tomikubo and K. Otsuka, *J. Catal.*, 2003, **219**, 176–185.
25 W. Wen, J. E. Calderon, J. L. Brito, N. Marinkovic, J. C. Hanson and J. A. Rodriguez, *J. Phys. Chem. C*, 2008, **112**, 2121–2128.
26 V. M. G. DelaCruz, J. P. Holgado, R. Pereñíguez and A. Caballero, *J. Catal.*, 2008, **257**, 307–314.
27 M. G. Zimicz, S. A. Larrondo, R. J. Prado and D. G. Lamas, *Int. J. Hydrogen Energy*, 2012, **37**, 14881–14886.
28 K. Kaneko and Y. Tamaura, *J. Phys. Chem. Solids*, 2009, **70**, 1008–1014.
29 K. Chayakul, T. Srithanratana and S. Hengrasme, *Catal. Today*, 2011, **175**, 420–429.
30 J. Zhang, Z. Wu, T. Liu, T. Hu, Z. Wu and X. Ju, *J. Synchrotron Radiat.*, 2001, **8**, 531–532.
31 S. Ricote, G. Jacobs, M. Milling, Y. Ji, P. M. Patterson and B. H. Davis, *Appl. Catal., A*, 2006, **303**, 35–47.
32 *Powder Diffraction File (PDF)*, Joint Committee on Powder Diffraction Standards (JCPDS), International Center of Diffraction Data (ICDD), Pennsylvania, USA, 1994 (CD ROM).
33 C. Diagne, H. Idriss and A. Kiennemann, *Catal. Commun.*, 2002, **3**, 565–571.
34 L. M. Martinez, M. Araque, J. C. Vargas and A. C. Rogera, *Appl. Catal., B*, 2013, **132–133**, 499–510.
35 J. Kaspar, P. Fornasiero, G. Balducci, R. Di Monte, H. Hickey and V. Sergo, *Inorg. Chim. Acta*, 2003, **349**, 217–226.
36 J. D. A. Bellido, E. Y. Tanabe and E. M. Assaf, *Appl. Catal., B*, 2009, **90**, 485–488.
37 J. I. Gutierrez-Ortis, B. Rivas, R. L. Fonseca and J. R. G. Velasco, *Appl. Catal., A*, 2004, **269**, 147–155.
38 K. Kamonsuangkasem, S. Therdthianwong and A. Therdthianwong, *Fuel Process. Technol.*, 2013, **106**, 695–703.
39 M. R. Nimlos, S. J. Blanksby, X. Qian, M. E. Himmel and D. K. Johnson, *J. Phys. Chem. A*, 2006, **110**, 6145–6156.

40 T. A. Semelsberger and R. L. Borup, *J. Power Sources*, 2006, **155**, 340–352.

41 C. D. Dave and K. K. Pant, *Renewable Energy*, 2011, **36**, 3195–3202.

42 X. Wang, M. Li, M. Wang, H. Wang, S. Li, S. Wang and X. Ma, *Fuel*, 2009, **88**, 2148–2153.

43 S. Adhikari, S. D. Fernando, S. D. F. To, R. M. Bricka, P. H. Steele and A. Haryanto, *Energy Fuels*, 2008, **22**, 1220–1226.

44 M. Araque, L. M. Martínez, T. , J. C. Vargas and A. C. Roger, *Catal. Today*, 2011, **176**, 352–356.

45 J. Chen, Q. Wu, J. Zhang and J. Zhang, *Fuel*, 2008, **87**, 2901–2907.

46 H. Song and U. S. Ozkan, *J. Catal.*, 2009, **261**, 66–74.

47 T. A. Maia, J. M. Assaf and E. M. Assaf, *Mater. Chem. Phys.*, 2012, **132**, 1029–1034.

48 S. Shao, A. W. Shi, C. L. Liu, R. Z. Yang and W. S. Dong, *Fuel Process. Technol*, 2014, **125**, 1–7.

49 K. Y. Koo, H. S. Roh, Y. T. Seo, D. J. Seo, W. L. Yoon and S. B. Park, *Appl. Catal., A*, 2008, **340**, 183–190.

50 J. W. Lee and C. Z. Li, *Carbon*, 2008, **46**, 1208–1217.